Letters

Identification of Resonance and Instability From Algebraic Virtual Impedance of Grid-Forming Control in the Perspective of Negative Sequence

Jaekeun Lee, *Graduate Student Member, IEEE*, Junyeol Maeng, *Graduate Student Member, IEEE*, Jae-Jung Jung, *Member, IEEE*, and Shenghui Cui, *Member, IEEE*

***Abstract*—Virtual impedance (VI) is commonly implemented in a static manner, typically neglecting the derivative term. This letter investigates fundamental issues associated with algebraic virtual impedance (AVI), emphasizing its characteristics related to negative-sequence impedance. The analysis reveals that AVI exhibits capacitive behavior in the negative-sequence impedance, inducing significant harmonic currents near a particular negative resonant frequency. Furthermore, the influence of control delay is analyzed, illustrating that AVI can readily become nonpassive within the negative-frequency region of the frequency domain, leading to harmonic instability. Experimental results are provided to validate the theoretical analysis.**

***Index Terms*—Negative-sequence component, passivity, resonance, stability, virtual impedance (VI).**

I. Introduction

In RECENT years, virtual impedance (VI) control has been widely employed for various purposes [1], including the improvement of power-sharing capabilities [2] and current-limiting control for grid-forming (GFM) inverters [3], [4]. A GFM inverter incorporating VI can be represented as an internal voltage source (IVS) behind a VI. Notably, an inductive VI is preferred for GFM capability [5], hence, VI should emulate virtual resistance and inductance.

Let v_o, e, and i be the output voltage, IVS, and inverter current, respectively, with subscripts α and β indicating their components in the stationary reference frame. With complex space vector representation, denoted by boldface letters, these can be expressed as $\mathbf{v}_o^s = v_{o,\alpha} + jv_{o,\beta}$, $\mathbf{e}^s = e_\alpha + je_\beta$, and $\mathbf{i}^s = i_\alpha + ji_\beta$. If a physical inductor is emulated, the relation can be described as

$$\mathbf{v}_o^s = \mathbf{e}^s - \left(R_v \mathbf{i}^s + L_v \frac{d\mathbf{i}^s}{dt}\right) \tag{1}$$

where R_v and L_v represents the virtual resistance and inductance, respectively. This method of implementation of VI will be referred to as differential VI (DVI). However, direct implementation of (1) is impractical due to the necessity of digital differentiator.

Meanwhile, an inductor with inductance L_v exhibits an impedance of $j\omega_1 L_v$ at the fundamental frequency, where ω_1 denotes the fundamental angular frequency. By considering only this positive-sequence fundamental-component impedance characteristic, the VI can be approximated as $j\omega_1 L_v$ and implemented in a three-phase system. Thereby, a commonly adopted simplified VI approach uses the following relationship [1], neglecting the derivative term

$$\begin{bmatrix} v_{o,\alpha} \\ v_{o,\beta} \end{bmatrix} = \begin{bmatrix} e_\alpha \\ e_\beta \end{bmatrix} - \begin{bmatrix} R_v & -X_v \\ X_v & R_v \end{bmatrix} \begin{bmatrix} i_\alpha \\ i_\beta \end{bmatrix} \tag{2}$$

where $X_v = \omega_1 L_v$ denotes the virtual reactance. This simplified approach will be referred to as algebraic VI (AVI).

In this letter, a symmetric three-phase system is considered, thereby allowing the well-established analytic methods from [6] and [7] to be employed. Utilizing complex space vector representation, (2) can be represented as

$$\mathbf{v}_o^s = \mathbf{e}^s - (R_v + jX_v)\,\mathbf{i}^s. \tag{3}$$

In (3), the constant term $R_v + jX_v$ itself is a complex transfer function, validating the relationship in both time- and frequency-domain analyses.

Despite its simplicity of implementation, AVI has occasionally been reported to exhibit instability [3], [4], [8]. Meanwhile, the negative-sequence impedance characteristic of AVI has largely been overlooked in previous research. As demonstrated in [7], negative-sequence impedance can be readily identified through frequency-domain analysis in the negative-frequency range.

This letter addresses the fundamental issue associated with AVI by closely examining its negative-sequence impedance

Received 25 March 2025; revised 27 April 2025; accepted 13 May 2025. Date of publication 19 May 2025; date of current version 5 August 2025. This work was supported by the Korea Institute of Energy Technology Evaluation and Planning, Korea Government (MOTIE), under Grant 20224000000160 (DC Grid Energy Innovation Research Center) and Grant RS-2023-00233148 (Development of Grid-Forming Topology and Inverter Core Technology for Grid Access to Distributed Energy Resources). *(Corresponding authors: Shenghui Cui; Jae-Jung Jung.)*

Jaekeun Lee, Junyeol Maeng, and Shenghui Cui are with the Department of Electrical and Computer Engineering, and with the SNU Electric Power Research Institute, Seoul National University, Seoul 08826, Republic of Korea (e-mail: jaek709@snu.ac.kr; junyul7@snu.ac.kr; cuish@snu.ac.kr).

Jae-Jung Jung is with the School of Electronic and Electrical Engineering, Kyungpook National University, Daegu 41566, Republic of Korea (e-mail: jj.jung@knu.ac.kr).

Color versions of one or more figures in this article are available at https://doi.org/10.1109/TPEL.2025.3571387.

Digital Object Identifier 10.1109/TPEL.2025.3571387

characteristic. First, it is demonstrated that AVI exhibits capacitive behavior in the negative-sequence components, potentially inducing significant harmonic currents under distorted grid voltage conditions. Furthermore, it is shown that AVI is particularly susceptible to losing passivity due to control delays in the negative-frequency region compared to the positive-frequency region, thereby introducing a higher risk of harmonic instability.

The rest of this article is organized as follows. The distinction between physical (differential) inductance and the algebraic inductance is discussed in Section II. Section III demonstrates the effect of equivalent series *LC* circuit in the negative-sequence domain when employing AVI. Section IV details the instability caused by control delay in AVI using impedance-based analysis. Finally, Section V concludes this article.

II. Distinction Between DVI and AVI

This section highlights the differing effects of DVI and AVI on the negative-sequence components. A general grid condition comprising both positive- and negative-sequence components is considered for the following reasons:

1) Negative-sequence components commonly exist in practical grid conditions. For instance, nonlinear electronic loads introduce negative-sequence harmonic currents into the grid, resulting in background harmonic voltages of the grid. Notably, harmonic orders of the form $6n+5$, such as the 5th and 11th harmonics, appear as negative-sequence components.
2) Although the negative-sequence voltage components in the grid may be initially negligible, the analysis in Section III demonstrates that even slight distortions in grid voltage can lead to significant negative-sequence currents when AVI is employed. Thus, negative-sequence current components shall be included in the analysis.
3) The impedance-based stability analysis in Section IV inherently requires consideration of all frequency components. This stability analysis is valid regardless of whether the background negative-sequence voltage components are explicitly present.

For these reasons, the subsequent analyses are conducted considering both positive- and negative-sequence components as a general case.

In this letter, subscript p and n denote positive- and negative-sequence components, respectively. Consider a current composed of positive- and negative-sequence components at angular frequency $\omega > 0$, given by $\mathbf{i}^s = \mathbf{i}^s_p + \mathbf{i}^s_n$, where $\mathbf{i}^s_p = I_p e^{j\phi_p} e^{+j\omega t}$ and $\mathbf{i}^s_n = I_n e^{j\phi_n} e^{-j\omega t}$. The magnitude and phase are represented by I and ϕ, respectively. Note that this expression represents the general form of the current component at angular frequency ω, encompassing both positive- and negative-sequence components. The special case in which no negative-sequence component is present corresponds to $I_n = 0$. If a physical inductance L_v is emulated, the following relationship holds:

$$L_v \frac{d\mathbf{i}^s}{dt} = L_v \left(j\omega I_p e^{\phi_p} e^{+j\omega t}\right) + L_v \left(-j\omega I_n e^{\phi_n} e^{-j\omega t}\right)$$

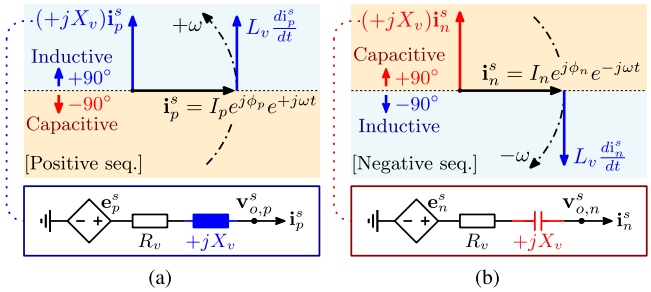

Fig. 1. Equivalent (a) positive-sequence circuit and (b) negative-sequence circuit comprising IVS and AVI. jX_v is inductive in (a) and capacitive in (b).

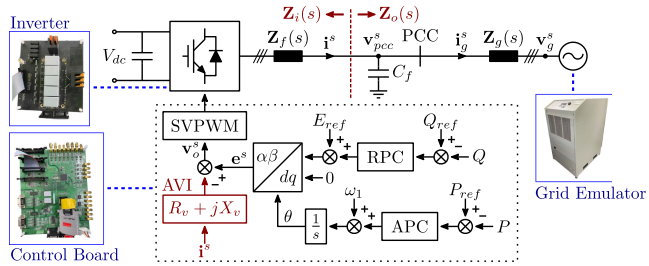

Fig. 2. System and control diagram.

$$= (+j\omega L_v)\mathbf{i}^s_p + (-j\omega L_v)\mathbf{i}^s_n. \tag{4}$$

This introduces phase shifts of $+90°$ and $-90°$ for positive- and negative-sequence components, respectively. Thus, for negative-sequence components, negative phase-shift response corresponds to inductive behavior. This outcome is expected since sL_v is a real transfer function. For a real transfer function $G(s)$, odd symmetry $\angle G(-j\omega) = -\angle G(j\omega)$ holds. However, this does not generally apply to complex transfer function [7].

On the contrary, the virtual reactance of AVI applies identical operation to both sequence components

$$jX_v\mathbf{i}^s = (+jX_v)\mathbf{i}^s_p + (+jX_v)\mathbf{i}^s_n. \tag{5}$$

Unlike (4), a uniform $+90°$ phase shift is applied to both positive- and negative-sequence components. Consequently, $(+jX_v)$ can be interpreted as a negative inductance, or equivalently, capacitance in the negative-sequence domain.

Fig. 1 illustrates the sequence-wise equivalent circuits of AVI employing $R_v + jX_v$. The phase shift demonstrates odd symmetry for differential inductance in DVI, whereas it exhibits even symmetry for algebraic inductance in AVI. Consequently, AVI appears inductive in the positive-sequence circuit but exhibits capacitive behavior in the negative-sequence circuit.

This letter identifies two critical issues arising from the capacitive nature of AVI in the negative-frequency region, which are elaborated in Sections III and IV, respectively:

1) harmonic resonance from equivalent *LC* circuit;
2) degradation of passivity and stability resulting from the effect of control delay in the negative-frequency region.

The analyses presented in the following sections are based on the system depicted in Fig. 2. $\mathbf{Z}_f(s)$ and $\mathbf{Z}_g(s)$ represent the impedances of the filter and grid inductors, respectively,

TABLE I
SYSTEM AND CONTROLLER PARAMETERS

Symbol	Parameter	Nominal Value
P_{rated}	Rated power	3 kW
ω_1	Nominal angular frequency	377.0 rad/s
f_{sw}	Switching frequency	10 kHz
V_{dc}	DC-link voltage	400 V
V_g	Grid voltage (line to line)	220 V
L_f	Filter inductance	3.4 mH
C_f	Filter capacitance	6 μF
H	Inertial time constant	3 s
ω_q	Cutoff frequency of LPF for RPC	314.2 rad/s
k_q	$Q-V$ droop gain	0.05 p.u.

and C_f represents the capacitance of the filter capacitor. $\mathbf{Z}_i(s)$ and $\mathbf{Z}_o(s)$ represent the inverter-side and point-of-common-coupling (PCC)-side equivalent impedances, respectively. The complex space vectors for grid voltage, PCC voltage, and grid-side current in a stationary reference frame are denoted as $\mathbf{v}_g^s$, $\mathbf{v}_{pcc}^s$, and $\mathbf{i}_g^s$, respectively. Synchronous power control [9] is implemented for active power control (APC), while droop control with a low-pass filter (LPF) is utilized for reactive power control (RPC). This configuration ensures slow dynamics of IVS, enhancing GFM capability. Thus, the influence of the outer control loop at harmonic frequencies is negligible. Detailed parameters are listed in Table I.

III. HARMONIC RESONANCE FROM EQUIVALENT *LC* CIRCUIT IN NEGATIVE SEQUENCE

This section describes the effect of equivalent *LC* circuit that emerges within $\mathbf{Z}_i(s)$ when AVI is employed.

A. Formulation of Equivalent LC Circuit by AVI

Neglecting control delay and parasitic resistance, consider the inverter-side impedance $\mathbf{Z}_i(s)$ composed of the filter inductance L_f and AVI, represented as

$$\mathbf{Z}_i(s) = R_v + jX_v + sL_f. \tag{6}$$

In the perspective of negative sequence, the $+jX_v$ term appears capacitive, resulting in an equivalent *LC* circuit configuration. At the negative angular frequency $-\omega_r$, satisfying

$$s = -j\omega_r = -jX_v/L_f \tag{7}$$

the term $jX_v + sL_f$ becomes zero, indicating an *LC* resonance condition.

A case study is conducted under conditions with a short-circuit ratio (SCR) of 50. Fig. 3(a) illustrates the impedance of $\mathbf{Z}_i(s)$ when DVI is applied with $L_v = 21.4$ mH and an X/R ratio of 5. $\mathbf{Z}_i(s)$ consistently exhibits inductive characteristics across both positive- and negative-frequency regions. In contrast, Fig. 3(b) shows the impedance of $\mathbf{Z}_i(s)$ under AVI implementation with $X_v = \omega_1 \times (21.4\ \text{mH})$ and an X/R ratio of 5. Here, the $\mathbf{Z}_i(s)$ exhibits capacitive characteristics within the negative-frequency region between -377.6 and 0 Hz. Also, the amplitude dip is observed at -377.6 Hz, as predicted by (7).

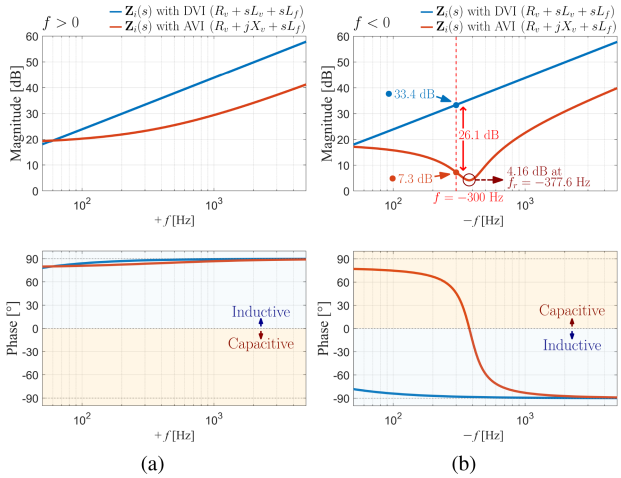

Fig. 3. Impedance plot of $\mathbf{Z}_i(s)$ with DVI and AVI for (a) positive frequency ($f > 0$) and (b) negative frequency ($f < 0$). $L_v = 21.4$ mH, $X_v = \omega_1 \times (21.4\,\text{mH})$, and X/R ratio is 5.

The low impedance magnitude of $\mathbf{Z}_i(s)$ near the resonant frequency f_r induced by AVI indicates that even a small background harmonic voltage of the grid can excite large harmonic current. In this case when the resonant frequency is -377.6 Hz, the GFM inverter with AVI is likely to introduce harmonic current when the grid voltage includes the negative-sequence fifth-order harmonic component ($f = -300$ Hz). As mentioned in Section II, the fifth-order harmonic component appear as negative sequence. At $f = -300$ Hz, the magnitude of $\mathbf{Z}_i(s)$ with DVI is 33.4 dB, while it is only 7.3 dB for the case with AVI. This indicates the AVI-assembled GFM inverter is vulnerable to the resonance at $f = -300$ Hz.

B. Experimental Verification Under Distorted Grid Voltage

A GFM inverter assembled with the AVI in conditions described above is connected to a distorted grid, whose voltage contains a fifth-order harmonic component of 0.025 p.u. appearing as a negative-sequence component. As shown in Fig. 3(b), the significantly attenuated impedance magnitude of $\mathbf{Z}_i(s)$ at $f = -300$ Hz, which is very close to the resonance frequency indicated by (7), would induce a significant fifth-order harmonic current when AVI is employed. For verification, it is compared against a scenario where a physical inductor with an inductance of 21.4 mH is added to L_f.

Fig. 4 illustrates the experimental results. The active and reactive power references are set to 1 and 0 p.u., respectively, and the sampling frequency of the digital controller of the GFM inverter is 20 kHz. Fig. 4(a) presents the scenario employing the physical inductor, demonstrating negligible harmonic current (THD $= 0.8\%$). In contrast, Fig. 4(b) illustrates that employing AVI significantly induces the fifth-order harmonic current to 1.12 A rms per phase (THD $= 19.7\%$), confirming the impact of the capacitive characteristic in negative-frequency region exhibited by AVI.

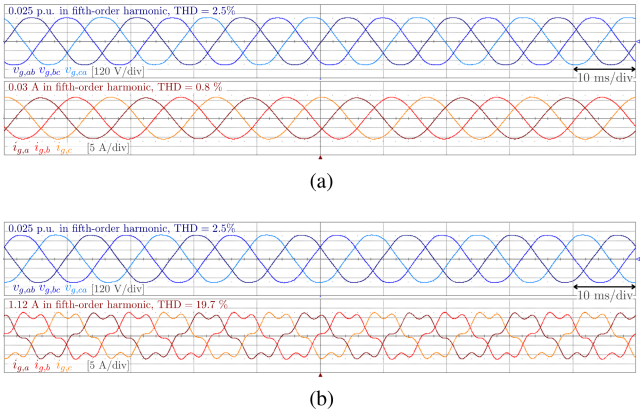

Fig. 4. Experimental result under distorted grid voltage, when (a) physical inductor is added, and (b) AVI is applied. SCR = 50, $L_v = 21.4\,\text{mH}$, $X_v = \omega_1 \times (21.4\,\text{mH})$, and X/R ratio is 5.

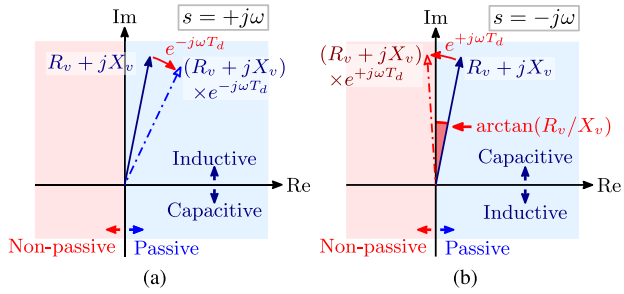

Fig. 5. Frequency-wise phasor diagram of AVI under control delay, for (a) positive-frequency component ($s = +j\omega$), (b) negative-frequency component ($s = -j\omega$).

IV. Stability Impact of Control Delay to AVI

This section analyzes the impact of control delay on AVI. First, it is demonstrated that passivity can readily be lost in the negative-frequency region. Subsequently, an impedance-based stability analysis incorporating nonpassive AVI characteristics is examined.

A. Effect of Control Delay on the Passivity of AVI

The passivity of VI is an important indicator of system stability. A VI characterized by transfer function $\mathbf{Z}_{VI}(s)$ is considered passive if the real part of $\mathbf{Z}_{VI}(j\omega)$ is nonnegative for all frequencies between $\pm f_s/2$, where f_s denotes the sampling frequency of the digital controller [10]. However, in the presence of control delay, the VI may lose passivity beyond a certain critical frequency. For the stability, it is desirable for the VI to maintain passivity (i.e., $\Re\text{e}[\mathbf{Z}_{VI}(j\omega)] \geq 0$) across a broad frequency range as much as possible. In this letter, both positive- and negative-frequency ranges are considered, since $\mathbf{Z}_{VI}(j\omega)$ is a complex transfer function. In general, $\Re\text{e}[\mathbf{Z}_{VI}(j\omega)] \neq \Re\text{e}[\mathbf{Z}_{VI}(-j\omega)]$, and thus, symmetry in the real part cannot be assumed.

Given a control delay T_d, the complex transfer function of delay-subjected AVI is expressed as

$$(R_v + jX_v)\, e^{-sT_d}. \tag{8}$$

For an angular frequency $\omega > 0$, (8) becomes $(R_v + jX_v)\, e^{-j\omega T_d}$ and $(R_v + jX_v)e^{+j\omega T_d}$, at $s = +j\omega$ and $s = -j\omega$, respectively. Fig. 5 depicts the phasor diagrams of (8) for each cases. Here, the sign of the real part determines the passivity.

When only the positive-frequency region is considered, (8) appears to maintain an adequate passivity margin, as depicted in Fig. 5(a). However, since (8) is inherently a complex transfer function, the corresponding phasor diagrams becomes asymmetric between the positive- and negative-frequency regions, as illustrated in Fig. 5(a) and (b). If the control delay is neglected, the phasor of $R_v + jX_v$ inherently aligns with the positive imaginary axis at all frequency components. Meanwhile, the phase shift introduced by the control delay exhibits odd symmetry with respect to positive and negative frequencies. As a result, control delay influences passivity differently across positive- and negative-frequency regions. Therefore, the negative-frequency region must be analyzed independently to accurately assess the passivity margin.

The sign of the real part of $(R_v + jX_v)e^{-sT_d}$ determines the passivity. In the positive-frequency region, where $s = +j\omega$ and $\omega > 0$, the real part is given by

$$\begin{aligned}&\Re\text{e}\left[(R_v + jX_v)\, e^{-j\omega T_d}\right] \\ &= \sqrt{R_v^2 + X_v^2} \cdot \sin\left(\arctan\left(R_v/X_v\right) + \omega T_d\right).\end{aligned} \tag{9}$$

Then the condition $\Re\text{e}[(R_v + jX_v)e^{-j\omega T_d}] \geq 0$ holds when

$$\omega \leq \pi/T_d - \arctan\left(R_v/X_v\right)/T_d. \tag{10}$$

Note that for GFM capability, it is generally recommended that $X_v \gg R_v$ [5], resulting $\arctan(R_v/X_v) \ll \pi/2$.

In the negative-frequency region, where $s = -j\omega$ and $\omega > 0$, the real part of $(R_v + jX_v)e^{-sT_d}$ is

$$\begin{aligned}&\Re\text{e}\left[(R_v + jX_v)\, e^{+j\omega T_d}\right] \\ &= \sqrt{R_v^2 + X_v^2} \cdot \sin\left(\arctan\left(R_v/X_v\right) - \omega T_d\right).\end{aligned} \tag{11}$$

In this case, $\Re\text{e}[(R_v + jX_v)e^{+j\omega T_d}] \geq 0$ holds only when

$$\omega \leq \arctan\left(R_v/X_v\right)/T_d. \tag{12}$$

Due to this asymmetry, the passivity margin significantly reduces in the negative-frequency region, as depicted in Fig. 5(b). This determines the critical frequency for passivity, f_c, as

$$f_c = \arctan\left(R_v/X_v\right)/(2\pi T_d) \tag{13}$$

which satisfies $\Re\text{e}[(R_v + jX_v)e^{+j2\pi f_c T_d}] = 0$. For the negative frequency below $-f_c$, (8) falls into nonpassive region.

To analyze the impact of control delay, two scenarios with different sampling frequencies (f_s) are considered: sampling at twice the switching frequency ($f_s = 2f_{sw}$) and at the switching frequency ($f_s = f_{sw}$), with the switching frequency fixed at 10 kHz. The control delay T_d is assumed as 1.5 times the sampling period [11], yielding 75 and 150 μs for sampling frequencies of 20 and 10 kHz, respectively. In this analysis, X_v is set to $\omega_1 \times$(15 mH) with an X/R ratio of 5. From (13), $-f_c$ is determined as -209.4 and -418.9 Hz, respectively, indicating a reduced passivity margin with increased control delay.

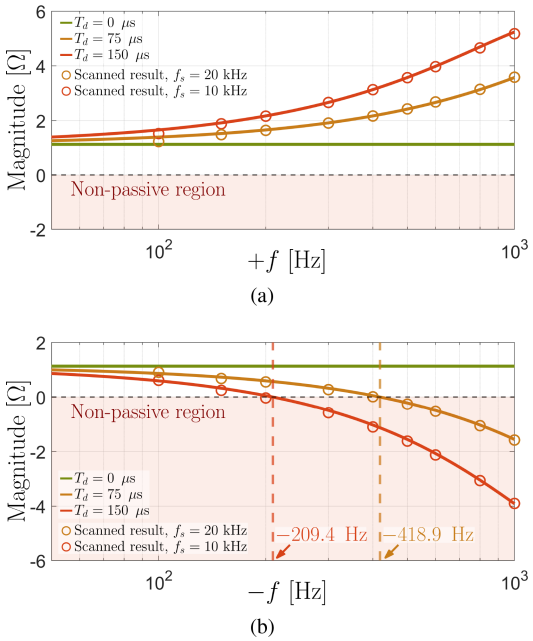

Fig. 6. Theoretical plot of $\Re\mathrm{e}[(R_v + jX_v)e^{-j2\pi f T_d}]$ and scanned measurement in (a) positive frequency ($f > 0$) and (b) negative frequency ($f < 0$). $X_v = \omega_1 \times$(15 mH) and X/R ratio is 5.

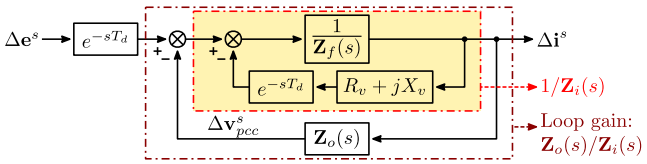

Fig. 7. Diagram of the open-loop transfer function $\mathbf{Z}_o(s)/\mathbf{Z}_i(s)$ under investigation, considering the control delay.

Simulation results verifying the passivity of delay-subjected AVI are presented in Fig. 6. The theoretical real part of the delay-subjected AVI is illustrated by solid lines, whereas the circles represent the scanned impedance result obtained from PLECS simulation. The simulation results closely match the theoretical predictions, confirming that the AVI exhibits nonpassive behavior for negative-sequence components below the critical negative frequency $-f_c$. In the positive-frequency region ($f > 0$), passivity is maintained up to the highest frequency evaluated. In contrast, in the negative-frequency region ($f < 0$), the response becomes nonpassive more readily. In addition, the results verify that increasing the control delay significantly reduces the passivity margin, particularly in the negative-frequency region.

B. Impedance-Based Stability Analysis

The nonpassive control loop can induce instability, which can be assessed through impedance-based analysis [12]. Under weak-grid condition (SCR of 2), the open-loop transfer function $\mathbf{Z}_o(s)/\mathbf{Z}_i(s)$, illustrated in Fig. 7, is analyzed. The open-loop

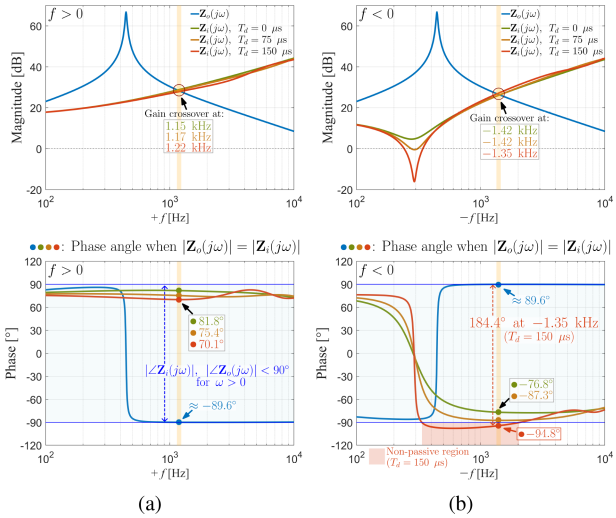

Fig. 8. Impedance plot of $\mathbf{Z}_o(s)$ and $\mathbf{Z}_i(s)$, under various control delay T_d, in (a) positive frequency ($f > 0$) and (b) negative frequency ($f < 0$). SCR = 2, $X_v = \omega_1 \times$(15 mH), and X/R ratio is 5.

transfer function $\mathbf{Z}_o(s)/\mathbf{Z}_i(s)$ characterizes the interaction between the grid and the inverter from an impedance perspective. By assessing the gain and phase margins of $\mathbf{Z}_o(s)/\mathbf{Z}_i(s)$, the potential risk of harmonic instability can be effectively evaluated. For accurate analysis in harmonic frequency range, the filter inductor is represented by an equivalent circuit model derived from impedance measurements, thereby capturing additional damping introduced by skin effect [13]. Incorporating the control delay, $\mathbf{Z}_i(s)$ is expressed as

$$\mathbf{Z}_i(s) = (R_v + jX_v)\, e^{-sT_d} + \mathbf{Z}_f(s). \tag{14}$$

$\mathbf{Z}_o(s)$ represents the PCC-side equivalent impedance, incorporating the filter capacitance C_f and the grid impedance $\mathbf{Z}_g(s)$. Thus, the following relationship holds:

$$1/\mathbf{Z}_o(s) = 1/\mathbf{Z}_g(s) + sC_f \tag{15}$$

and therefore $\mathbf{Z}_o(s)$ is expressed as

$$\mathbf{Z}_o(s) = \mathbf{Z}_g(s)/\left(1 + sC_f\mathbf{Z}_g(s)\right). \tag{16}$$

Let $s = j\omega = j(2\pi f)$, where f can be either positive or negative. Fig. 8 presents impedance plots of $\mathbf{Z}_i(j\omega)$ and $\mathbf{Z}_o(j\omega)$. As depicted in Fig. 8(a), both $\mathbf{Z}_i(j\omega)$ and $\mathbf{Z}_o(j\omega)$ exhibit passive behavior in the positive-frequency region, showing no indication of instability. In contrast, the red-highlighted region in Fig. 8(b) illustrates a nonpassive region in $\mathbf{Z}_i(j\omega)$ at negative frequencies for the largest considered control delay, namely 150 μs. For the other cases with smaller control delays, i.e., 75 and 0 μs, $\mathbf{Z}_i(j\omega)$ remains passive over the examined frequency range, indicating stability over the evaluated range.

At the gain crossover frequency, the phase difference between $\mathbf{Z}_i(j\omega)$ and $\mathbf{Z}_o(j\omega)$ is assessed to determine the phase margin. For the case with the sampling frequency of 10 kHz, the gain crossover occurs at $f = -1.35$ kHz, where the phase difference $\angle\mathbf{Z}_o(j\omega) - \angle\mathbf{Z}_i(j\omega)$ is determined to be 184.4°. This

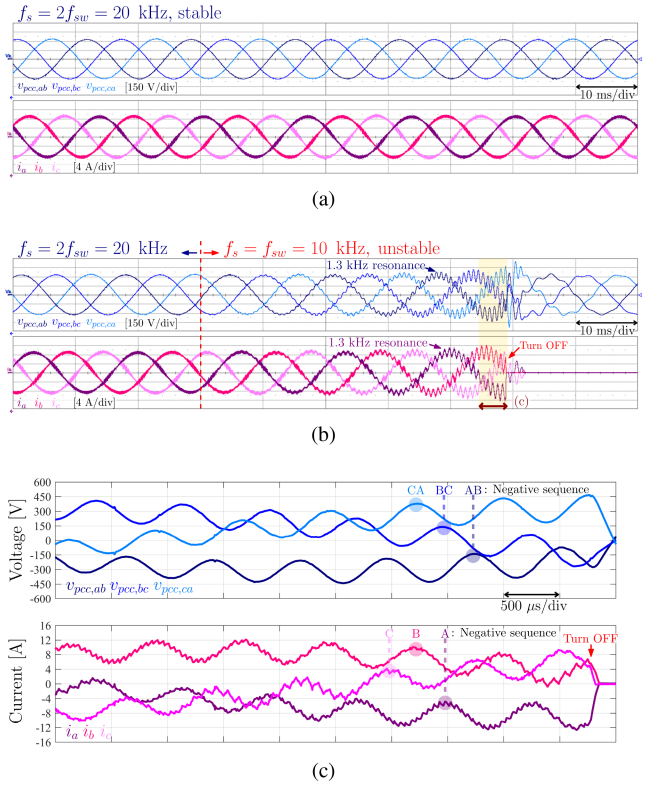

Fig. 9. Experimental result with AVI, for (a) $f_s = 2f_{sw} = 20$ kHz, stable. (b) For $f_s = f_{sw} = 10$ kHz, unstable. (c) Magnified view of the highlighted region in (b). SCR $= 2$, $X_v = \omega_1 \times$(15 mH), and X/R ratio is 5.

corresponds to a negative phase margin of -4.4° for the loop gain $\mathbf{Z}_o(s)/\mathbf{Z}_i(s)$, indicating instability.

C. Experimental Verification of Control Delay Effect

Fig. 9 presents experimental results under the previously described conditions. Active power and reactive power references are set to 0.8 and 0.2 p.u., respectively. Fig. 9(a) demonstrates stable operation with the sampling frequency of 20 kHz. Conversely, Fig. 9(b) reveals instability triggered by reducing the sampling frequency to 10 kHz, which aligns with the theoretical predictions. Additionally, the experimental result exhibits harmonic oscillations around 1.3 kHz, which closely coincide with the gain crossover frequency identified in Fig. 8(b). A magnified view of the highlighted region in Fig. 9(b) is depicted in Fig. 9(c). The closer inspection confirms that the 1.3 kHz harmonic resonance manifests as a negative-sequence component, thereby validating the theoretical analysis.

V. Conclusion

This letter has identified and analyzed resonance and instability issues associated with AVI, demonstrating that these phenomena are particularly evident when examined in the negative-frequency region. Therefore, the negative-sequence impedance characteristics should be explicitly considered during the design process of AVI-based controllers. To ensure inductive characteristics and maintain passivity for both positive- and negative-sequence components, adoption of alternative VI methods is recommended, with particular attention to the impact of control delay.

References

[1] X. Wang, Y. W. Li, F. Blaabjerg, and P. C. Loh, "Virtual-impedance-based control for voltage-source and current-source converters," *IEEE Trans. Power Electron.*, vol. 30, no. 12, pp. 7019–7037, Dec. 2015.

[2] J. He, Y. W. Li, J. M. Guerrero, F. Blaabjerg, and J. C. Vasquez, "An islanding microgrid power sharing approach using enhanced virtual impedance control scheme," *IEEE Trans. Power Electron.*, vol. 28, no. 11, pp. 5272–5282, Nov. 2013.

[3] A. D. Paquette and D. M. Divan, "Virtual impedance current limiting for inverters in microgrids with synchronous generators," *IEEE Trans. Ind. Appl.*, vol. 51, no. 2, pp. 1630–1638, Mar./Apr. 2015.

[4] H. Wu and X. Wang, "Small-signal modeling and controller parameters tuning of grid-forming VSCs with adaptive virtual impedance-based current limitation," *IEEE Trans. Power Electron.*, vol. 37, no. 6, pp. 7185–7199, Jun. 2022.

[5] H. Wu, X. Wang, and L. Zhao, "Design considerations of current-limiting control for grid-forming capability enhancement of VSCs under large grid disturbances," *IEEE Trans. Power Electron.*, vol. 39, no. 10, pp. 12081–12085, Oct. 2024.

[6] S. Gataric and N. Garrigan, "Modeling and design of three-phase systems using complex transfer functions," in *Proc. 30th Annu. IEEE Power Electron. Specialists Conf. Record.*, 1999, pp. 691–697.

[7] L. Harnefors, "Modeling of three-phase dynamic systems using complex transfer functions and transfer matrices," *IEEE Trans. Ind. Electron.*, vol. 54, no. 4, pp. 2239–2248, Aug. 2007.

[8] A. Rodríguez-Cabero, J. Roldán-Pérez, and M. Prodanovic, "Virtual impedance design considerations for virtual synchronous machines in weak grids," *IEEE Trans. Emerg. Sel. Topics Power Electron.*, vol. 8, no. 2, pp. 1477–1489, Jun. 2020.

[9] P. Rodriguez, I. Candela, and A. Luna, "Control of PV generation systems using the synchronous power controller," in *Proc. IEEE Energy Convers. Congr. Expo.*, 2013, pp. 993–998.

[10] L. Harnefors, A. G. Yepes, A. Vidal, and J. Doval-Gandoy, "Passivity-based controller design of grid-connected VSCs for prevention of electrical resonance instability," *IEEE Trans. Ind. Electron.*, vol. 62, no. 2, pp. 702–710, Feb. 2015.

[11] L. Harnefors, X. Wang, A. G. Yepes, and F. Blaabjerg, "Passivity-based stability assessment of grid-connected VSCs—An overview," *IEEE Trans. Emerg. Sel. Topics Power Electron.*, vol. 4, no. 1, pp. 116–125, Mar. 2016.

[12] J. Sun, "Impedance-based stability criterion for grid-connected inverters," *IEEE Trans. Power Electron.*, vol. 26, no. 11, pp. 3075–3078, Nov. 2011.

[13] H. Matsumori, T. Shimizu, F. Blaabjerg, X. Wang, and D. Yang, "Stability influence of filter components parasitic resistance on LCL-filtered grid converters," in *Proc. Int. Power Electron. Conf.*, 2018, pp. 3357–3362.